Subthreshold ρ^0 photoproduction on ^{3}He

M. A. Kagarlis,* Z. Papandreou,† G. M. Huber, G. J. Lolos, A. Shinozaki, E. J. Brash, F. Farzanpay, M. Iurescu, and A. Weinerman
Department of Physics, University of Regina, Regina, Saskatchewan, Canada S4S 0A2

G. Garino‡ and K. Maruyama
Institute for Nuclear Study,§ University of Tokyo, Tanashi, Tokyo 188, Japan

O. Konno, K. Maeda, T. Terasawa, and H. Yamazaki
Department of Physics, Tohoku University, Sendai 980, Japan

T. Emura, H. Hirosawa, K. Niwa, and H. Yamashita
Department of Applied Physics, Tokyo University of Agriculture and Technology, Koganei, Tokyo 184, Japan

S. Endo, K. Miyamoto, and Y. Sumi
Department of Physics, Hiroshima University, Higashi-Hiroshima 724, Japan

A. Leone and R. Perrino
INFN-Sezione di Lecce, I-73100 Lecce, Italy

T. Maki
University of Occupational and Environmental Health, Kitakyushu 807, Japan

A. Sasaki
College of General Education, Akita University, Akita 010, Japan

J. C. Kim
Department of Physics, Seoul National University, Seoul 151-742, Korea

(TAGX Collaboration)

(Received 30 November 1998; published 9 July 1999)

A large reduction of the ρ^0 mass in the nuclear medium is reported, inferred from dipion photoproduction spectra in the 1 GeV region, for the reaction $^3\mathrm{He}(\gamma,\pi^+\pi^-)X$ with a 10% duty factor tagged-photon beam and the TAGX multiparticle spectrometer. The energy range spanned ($800 \leqslant E_\gamma \leqslant 1120$ MeV) lies mostly below the free-ρ^0 production threshold, a region which is believed to be sensitive to modifications of light vector-meson properties at nuclear-matter densities. The values of the ρ^0 mass extracted from the Monte Carlo fitting of the data were $m^*_{\rho^0} = 642 \pm 40$, 669 ± 32, and 682 ± 56 MeV/c^2 for E_γ in the 800–880, 880–960, and 960–1040 MeV regions, respectively. These values were independently corroborated in a qualitative fashion by a measured, assumption-free, kinematical observable. This mass shift, far exceeding current mean-field-driven theoretical predictions, may be suggestive of a nucleonic source of modification or of a bound state in the nuclear mean field. [S0556-2813(99)01608-8]

PACS number(s): 12.38.Qk, 13.60.Le, 25.20.Lj, 14.40.Cs

I. INTRODUCTION

Hadronic dynamics has until recently been comprised of two nonoverlapping domains, distinctly separated along the lines of their respective description of matter as hadronic or quark. On the low-energy side of the spectrum, matter is probed on a scale where pions and baryonic resonances are the relevant constituents. These have been rather successfully employed by quasiphenomenological models in providing prescriptions for free and in-medium hadronic interactions. At the higher-energy end, far above energies typical of baryonic resonances, quark degrees of freedom become accessible and matter tends asymptotically towards quark-gluon plasma. In this regime, described by perturbative QCD, quarks become deconfined and chiral symmetry is restored.

Although the origin of quark confinement is not known, it is evident that, whatever the reasons, it must induce spontaneous breaking of chiral symmetry [1]. The two phenomena are therefore linked and in the limit of chiral symmetry res-

*Present address: GSI, KPI/Leptonen, Planckstrasse 1, D-64291 Darmstadt, Germany.
†Corresponding author. Electronic address: zisis@latour.phys.uregina.ca
‡Present address: Department of Physics, University of Evansville, Evansville, Indiana 47722.
§Present name: KEK-Tanashi Division.

toration, as quark masses tend to zero, vector-meson masses and widths are also expected to change [2]. The transition from hadronic to quark matter and the effect of increasing the density and temperature on the properties of light vector mesons have been addressed in the context of QCD sum rules [3] as well as effective Lagrangians [4]. In particular, a temperature- and density-dependent lowering of the ρ^0 mass is regarded as a precursor of the chiral phase transition, expected to be measurable even at normal nuclear density [5]. Thus, the energy region from hadronic phenomenology to the domain of perturbative QCD has come to the foreground, as the study of vector-meson property modifications in this range appears to hold the key to understanding the mechanism of chiral symmetry restoration.

The recent advent of high-duty-cycle photon beams, on the one hand, and high-resolution dilepton spectrometers, on the other, have opened up the possibility of reconciliation between the hadronic and quark depictions of matter. Hadronic probes coupled with hadron spectrometers had been extensively used in the past for energies up to the Δ resonance, but higher up, where multipion production channels increasingly dominate, the combination becomes rapidly cumbersome due to medium distortions from initial and final state interactions. For the study of the vector mesons that couple to multipion states, the photon is ideally suited. For this reason, we have chosen a tagged-photon beam for our investigation. This paper is a followup to our earlier published results [6], and provides additional details on the experiment as well as results of an improved analysis.

A. Relativistic heavy-ion results

The quest to delineate the vector-meson field in the nuclear medium has generated activity in a variety of fields. At relativistic energies, under extreme conditions of temperature and density, the quest for signs of a phase transition from hadronic matter to quark-gluon plasma is at the heart of experimental programs using heavy-ion beams (e.g., at CERN, GSI, and RHIC) and dilepton spectrometers. A series of pioneering studies from the CERES, HELIOS-3, and NA50 Collaborations at SPS/CERN, with central S+Au, S+W, Pb+Au, and Pb+Pb collisions, have largely been interpreted as indicative of a downward shift of the ρ^0 mass in the nuclear medium [7,8]. The invariant mass spectra for dilepton production that have been measured in these experiments, when compared with the respective *p-A* spectra, show a large enhancement at low-invariant-mass regions. The excess dileptons are thought to originate from the decay of mesonic resonances produced in $\pi^+\pi^-$ annihilation and, in the mass region $0.2<m_{l^+l^-}<0.5$ GeV/c^2, the models advocating vector-meson medium modifications attribute the enhancement to the decay of the ρ^0 meson with a downward-shifted mass [9,10]. In another approach, an explanation in terms of conventional phenomenological ρ^0-meson medium modifications is also consistent with the CERN data [11–13]. In this more conservative approach, the ρ^0 spectral function below 0.6 GeV/c^2 in dilepton invariant mass is appreciably enhanced from the contributions of ''rhosobar''-type excitations such as the ΔN^{-1}, $N^*(1720)N^{-1}$, and $\Delta^*(1905)N^{-1}$, a consequence of the strong coupling of the ρ^0 meson with $\pi^+\pi^-$ states in the nuclear medium.

Another theoretical model, which combines chiral SU(3) dynamics with vector-meson dominance in an effective Lagrangian, has shown that chiral restoration does not demand a drastic reduction of vector-meson masses in the nuclear medium [14]. This model, in qualitative agreement with hadronic-phenomenological work [11,13], predicts a substantial enhancement of the ρ^0 spectral density below the nominal resonance mass, with only a marginal mass reduction. Moreover, an interpretation of the CERES data as the outcome of either medium-modified hadronic interactions or interactions of dissociated quarks in the quark-gluon phase yields consistent results in the framework of Ref. [14], leading to the conjecture that both the hadronic and quark-gluon phases must be present [14]. The latter conclusion is also drawn by a synthesis of the mass-scaling [5] and hadronic-phenomenological [13] models, leading to the prediction that dynamical-hadronic effects that are dominant up to about nuclear density, mainly via the highly collective $N^*(1520)N^{-1}$ state, gradually give way to ρ^0-meson mass scaling as the quark degrees of freedom become increasingly relevant.

Other less directly related experimental conjectures of medium modifications of the ρ^0 mass have been deduced from an anomalous J/ψ suppression, reported by the NA50 Collaboration for Pb+Pb collisions [15], enhanced K^+-^{12}C scattering cross sections [16], and an IUCF experiment of polarized proton scattering on ^{28}Si, though in the latter the medium renormalization of the ρ^0 mass required for agreement with the data is inconsistent for different observables measured in the same experiment [17].

In summary, the experimental results discussed so far are inconclusive with regard to the magnitude of the ρ^0-meson medium mass modification, and underline the limitations encountered in complex processes, where the probe interacts with nuclear matter via the strong interaction and the channel being investigated may not be disentangled from conventional medium effects.

B. Electromagnetic probe results

These difficulties are largely overcome with the use of photons, which do not suffer from initial state interactions. The availability of high-flux photon beams, which have compensated for the low interaction cross sections with nuclear matter, complemented by wide-angle multiparticle spectrometers, has made possible a new generation of experiments. In the $E_\gamma \sim 1$ GeV region, matter is probed at short distances ($\leqslant 1$ fm), which is at the gateway of the energy range where vector-meson properties are expected to undergo modifications. In this domain, baryons and mesons are still the relevant constituents for the description of matter, yet their quark content becomes increasingly manifest, a fact which is reflected in QCD-inspired phenomenological models [18,19]. The ρ^0 meson is the best candidate among the light vector mesons $\rho^{0,\pm}$, ω, and φ as a probe of medium modifications, since, due to its short lifetime and decay length (1.3 fm), a large portion of ρ^0 mesons produced on nuclei will decay in the medium.

For effective measurements with photons in the 1 GeV region, kinematically complete experiments are required, which in turn necessitate the use of high-duty-cycle tagged-photon beams and large-acceptance multiparticle spectrometers. These requirements were met by the TAGX detector [20] at the Institute for Nuclear Study (INS), where the TAGX Collaboration has completed a series of experiments on the $^3\mathrm{He}(\gamma,\pi^+\pi^-)X$ reaction with a 10%-duty-cycle tagged-photon beam. First, a lower-energy experiment ($380 \leqslant E_\gamma \leqslant 700$ MeV) measured the single- and double-Δ contributions to $\pi^+\pi^-$ production [21]. Having established these important non-ρ^0 dipion processes, the kinematics of the $^3\mathrm{He}(\gamma,\pi^+\pi^-)X$ reaction were investigated in the range $800 \leqslant E_\gamma \leqslant 1120$ MeV, aiming at the $\rho^0 \rightarrow \pi^+\pi^-$ channel.

Coherent ρ^0-meson photoproduction on nuclei is characterized by small four-momentum transfers, resulting in ρ^0 mesons which mostly decay outside of the nucleus [22] and are of limited utility in probing vector-meson medium modifications. The $800 \leqslant E_\gamma \leqslant 1120$ MeV region in this experiment was in fact chosen in order to largely suppress this process, which has a threshold of $E_\gamma \approx 1083$ MeV. On the other hand, for a nominal ρ^0 mass of 770 MeV/c^2, quasifree ρ^0 photoproduction is dominated by the $\gamma + N \rightarrow \rho^0 + N'$ reaction in the nuclear medium, and this process is relevant in the energy region of interest. For a ^{3}He target, the energy threshold of this process is $E_\gamma \approx 873$ MeV, whereas the 1083 MeV energy threshold of the elementary ρ^0 photoproduction reaction on a nucleon is lowered for the quasifree channel in the nuclear medium, as the Fermi momentum of the struck nucleon may be utilized to bring the ρ^0 meson on shell.

Quasifree subthreshold photoproduction ($E_\gamma < 1.083$ GeV) on the one hand warrants that the interaction took place in the interior of the nucleus, since the nucleon Fermi momentum is required to produce the ρ^0, and, on the other hand, produces slower ρ^0 mesons, also more likely to decay inside the nucleus. Moreover, this process can be investigated for two different final states, depending on whether the target nucleus remains bound in the final state (exclusive-quasifree channel) or decomposes to its constituent nucleons (breakup-quasifree channel). Both channels produce ρ^0 mesons which are slow relative to the struck object and may travel distances shorter than the nucleonic radius before decaying (Sec. V B). Thus, large densities in the interior of the nucleon may become accessible, amounting to a nucleonic medium effect, although a bound ρ^0 decaying within the nucleus may also result in the breakup of the nucleus even though the primary interaction is mean-field driven. It should be emphasized here that a nucleonic medium effect may also include the formation of a ''rhosobar'' state, which clearly involves the excitation of a nucleon to that state. In the deep subthreshold region, and for large momentum transfers to the target nucleus, the coherent and exclusive-quasifree channels are suppressed, and the breakup-quasifree process becomes dominant. It is this region that motivated the $800 \leqslant E_\gamma \leqslant 1120$ MeV ρ^0 photoproduction experiment.

The aim of the experiment being as stated above, the choice of ^{3}He as the target becomes almost ideal. The low photon energies utilized to induce subthreshold photoproduction result in slow ρ^0 mesons with a small Lorentz boost, and therefore a large probability for decay within the nuclear volume. Thus, in the case of the exclusive channel, a large nuclear radius is not necessary, and the larger nuclear density of a heavier target is predicted to have only a marginally enhanced effect on the ρ^0 meson mass [19]. Furthermore, if the breakup process is dominated by the nucleonic field, the size of the target nucleus is largely irrelevant. Finally, the ^{3}He target is the lightest nucleus where a nuclear medium effect may be discernible, without the complexity of overwhelming final state interactions (FSI's).

The ρ^0 detection is further aided by the inherent selectivity of the TAGX spectrometer (Sec. II B) to small-angle emission, for the primary reactions, leading to coplanar $\pi^+\pi^-$ processes [20]. This is due to the limited out-of-plane acceptance of the spectrometer, which preferentially selects the $\rho^0 \rightarrow \pi^+\pi^-$ channel, at the expense of two-step processes (e.g., FSI's) and uncorrelated $\pi^+\pi^-$ production at distinct reaction vertices, the latter accounting for the majority of non-ρ^0 background events (Sec. IV A). This favorable feature of the spectrometer promotes an otherwise small component of the total amplitude, namely, the subthreshold breakup channel, to a sizable experimental signal.

The mass of the ρ^0 meson in the nuclear medium was extracted from the dipion spectra of the $800 \leqslant E_\gamma \leqslant 1120$ MeV experiment with the aid of Monte Carlo (MC) simulations [6]. The reported mass shift was far larger than the predictions of any mean-field driven model pertaining to the exclusive process for ^{3}He [19]; a calculation based on QHD assuming a deep scalar potential yielding a ρ^0-^{3}He bound state, on the other hand, produced much better agreement [23]. Along similar lines, another theoretical work in Ref. [24] argues that the explicit inclusion of the tensor coupling of the ρ meson to the nucleon results in a large reduction of the ρ^0 mass, in general agreement with the observations of Refs. [6,25].

The result of Ref. [6] led to a reanalysis of the lower-energy measurements [21] including the $\rho^0 \rightarrow \pi^+\pi^-$ channel and allowing for ρ^0 production with a shifted mass. The outcome of this reanalysis was an even larger shift [25], possibly indicating a mechanism other than those previously considered. A nucleonic medium effect, as sketched earlier, may be consistent with a large ρ^0-mass reduction, although a theoretical model has yet to be fully developed for ^{3}He [26,27].

Though more work is needed to firmly establish and better understand these results [28], the $^3\mathrm{He}(\gamma,\pi^+\pi^-)X$ experiment for photon energies in the range $800 \leqslant E_\gamma \leqslant 1120$ MeV constitutes the first direct measurement of the ρ^0 mass in the nuclear medium. In this paper, a new and more thorough analysis is presented, including the first direct evidence of the characteristic $J=1$ signature of the ρ^0 meson decay in the subthreshold region, as well as refinements in the simulations and fitting procedure, relative to the analysis of Refs. [6,21,25], leading to higher confidence in the extraction of the in-medium ρ^0 mass.

The paper is organized in six sections. In Sec. II, the experimental setup and the calibration procedure are reviewed. In Sec. III the data-analysis algorithm is outlined in conjunction with the experimental aspects of Sec. II. Section

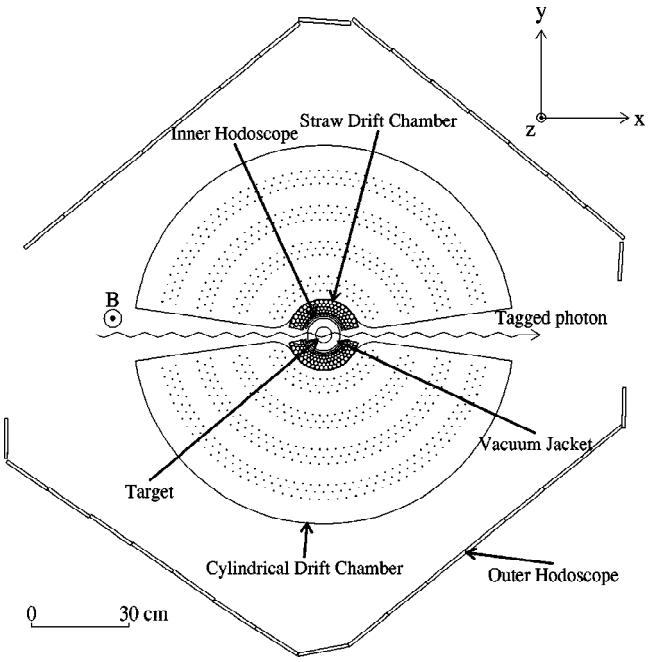

FIG. 1. Components of the TAGX spectrometer: Radially outwards from the target vessel at the center are seen the IH, SDC, CDC, and OH. The TAGX coordinate frame has the $\hat{x}$ axis pointing in the direction of the photon beam, and the $\hat{z}$ axis pointing outward from the page in the direction of the 0.5 T magnetic field of the dipole analyzer magnet. Veto counters (not shown in the figure) are positioned along the OH arms in the xy plane, for e^+e^--pair rejection, mainly at forward angles.

IV focuses on the MC techniques and the fitting of the data, leading to the extraction of the mass shift. In Sec. V the data are compared with the MC calculations, and the ρ^0-mass shifts are discussed. Finally, the conclusions are presented in Sec. VI.

II. APPARATUS

The INS tagged photon beam and the TAGX spectrometer (Fig. 1) [20], the new straw drift chamber [29], and different aspects of the data-analysis procedure [20,21] have all been described in detail elsewhere, where the reader is referred for a more extensive discussion. In this section, a brief overview of the experimental apparatus is provided, as it applies for the $^3\mathrm{He}(\gamma,\pi^+\pi^-)X$ measurements, stressing the elements that were either introduced for the first time in this experiment, or that are important for the data analysis.

A. Photon beam and ^{3}He target

The photon beam is produced utilizing the 1.3 GeV Tokyo Electron Synchrotron. A series of innovative technical improvements led, in 1987, to the upgrading of the photon beam to one of medium-duty cycle. In the present experiment, the end-point electron energy E_s is 1.22 GeV at an average 10% duty factor, corresponding to a 5 ms extraction time. The instantaneous energy of the extracted electrons has a sinusoidal dependence, and it is known by measuring the extraction time. The extracted electrons are directed via a beamline onto a thin platinum radiator where bremsstrahlung photons are produced, while the scattered electrons are bent away from the beam by a rectangular analyzer magnet of 1.17 T. The magnet settings of the extraction beamline vary sinusoidally in time, in phase with the E_s energy. An array of 32 scintillator electron-tagging counters, each with a 10 MeV/c momentum acceptance, detect the scattered electrons. The position of the tagger registering the scattered electron determines its energy and, consequently, that of the bremsstrahlung photon as $E_\gamma = E_e - E_{e'}$ with $\Delta E_\gamma \sim \pm 5$ MeV accuracy. A second set of 8 backing taggers participates in the coincidence triggering signal, along with the 32 frontal ones, and is discussed in the following section. The tagged photon intensity was maintained at an average of $\sim 3.5\times 10^5$ γ/s, well within the tolerance of the data acquisition system for accidental triggers. The photons, distributed over a beam spot of ~ 2 cm in diameter, are subsequently incident on a liquid ^{3}He target. The target is at a temperature of 1.986 ± 0.001 K, corresponding to a 0.0786 g/cm^3 density, and is contained in a cylindrical vessel 90 mm in height and 50 mm in diameter at the center of the TAGX spectrometer [30].

The tagger hits are related to the photon flux incident upon the target after efficiency corrections. In particular, due to the collimation of the photon beam downstream from the taggers, some of the tagged photons do not reach the target. To determine the tagging efficiency, and consequently the photon flux, a lead-glass Čerenkov counter is placed in the photon beam, with reduced flux, downstream from the target and the tagger scalers are periodically recorded both with and without the platinum radiator in place. The efficiency per tagger counter is determined by the relation

$$\eta_{l\in[1,32]} = \frac{[\check{C}\cdot T_l]_{\mathrm{in}} - [\check{C}\cdot T_l]_{\mathrm{out}} - [\check{C}_{\mathrm{acc}}\cdot T_l]_{\mathrm{in}}}{T_{l_{\mathrm{in}}} - T_{l_{\mathrm{out}}}}, \qquad (1)$$

where T_l is the scalar count for each of the frontal taggers. The term $[\check{C}\cdot T_l]_{\mathrm{out}}$ corresponds to the coincidences between a tagger-counter and a lead-glass Čerenkov hit from a spurious photon not originating from the platinum radiator, and $[\check{C}_{acc}\cdot T_l]_{\mathrm{in}}$ is the number of accidental coincidences with the radiator in place, but with the Čerenkov hit registering with a delay of the order of 100 ns with respect to the tagger counter signal. These two terms turn out to be negligible relative to the term $[\check{C}\cdot T_l]_{\mathrm{in}}$ in Eq. (1), which gives the efficiency-corrected number of tagged photons per tagger reaching the target as

$$N_{l\in[1,32]} = \eta_l T_{l_{\mathrm{in}}}\left(1 - \frac{T_{l_{\mathrm{out}}}}{T_{l_{\mathrm{in}}}}\right). \qquad (2)$$

The efficiencies η_l and radiator out/in ratios $\mathcal{R}_l = T_{l_{\mathrm{out}}}/T_{l_{\mathrm{in}}}$ for the 32 frontal taggers are recorded in a number of dedicated runs, in regular intervals throughout the experiment, and they are used, along with Eq. (2), in the empty-target background subtraction procedure applied to the measured spectra (see Sec. III).

B. Spectrometer

The TAGX spectrometer has an acceptance of π sr for charged particles (neutral-particle detection was not utilized in the present experiment), and has been in use at INS since 1987. It consists of several layers of detector elements (Fig. 1) positioned radially outwards from the target vessel, which is located at the center of the 0.5 T field of a dipole analyzer magnet.

Directly surrounding the target container is the inner hodoscope (IH), made up of two sets of six scintillator counters, one on each side of the beam. The IH is used in the trigger, as well as in measuring the time of flight (TOF) of the outgoing particles [20,29]. As it is placed inside a strong magnetic field, the light signal is carried by optical fibers to the photomultiplier tubes, which are located at the fringes of the magnetic field two meters away.

Next is the straw drift chamber (SDC), operating since 1994 and installed expressly for the measurement of the ρ^0 mass in ^{3}He, with the objective of improving the momentum resolution for the detection of the $\rho^0 \rightarrow \pi^+ \pi^-$ decay channel [29]. The SDC consists of two semicircular cylindrical sections, each containing four layers of vertical cells. The ''straw'' cells have tube-shaped cathodes which induce a radial electric field, and consequently have a regular field definition and high position resolution (~ 150 μm). The SDC was designed to preserve the π-sr large acceptance prior to its installation, to not impose extensive modifications of the spectrometer, and to not induce significant energy losses to traversing particles by keeping its thickness to minimum. The installation of the SDC required, nonetheless, the replacement of the IH from an earlier set of scintillators with the one described above.

Surrounding the SDC are two semicircular cylindrical drift chambers (CDC's) subtending angles from 15° to 165° on both sides of the beamline in the horizontal plane, and $\pm 18.3°$ in vertical out-of-plane angles. Each CDC is composed of 12 concentric layers of drift cells, yielding a ~ 250–300 μm horizontal and 1.5 cm vertical resolution. Together with the SDC, they are used to determine the planar momentum and emission angle of the charged particles traversing them, and the vertex position of trajectory crossings.

The outer set of 33 scintillator elements comes next, serving as the outer hodoscope (OH), with photomultiplier tubes (PMT's) attached at both ends to help determine the track angle relative to the median plane. The two sets of hodoscopes, IH and OH, measure the TOF corresponding to the tracked trajectories.

Other components of the TAGX spectrometer include four sets of 155 mm$\times$50 mm$\times$5 mm counters with a primary function to veto e^+e^- background. These veto counters are positioned along the OH arms in the median plane, and eliminate charged-particle tracks registering within $\Delta z = \pm 2.5$ mm, mostly affecting forward-focused e^+e^- pairs produced copiously downstream from the target, but having a small effect on $\pi^+\pi^-$ events.

C. Data acquisition and calibration

The channel of interest being $\pi^+\pi^-$ production from the decay of the ρ^0 meson, two-charged-particle coincidences on opposite sides of the beam axis were required of the trigger. Two levels of triggering are implemented in order to optimize the data acquisition electronics. The pretrigger

$$\mathcal{PT} = IH_L\, IH_R \sum_{i=1}^{8} \mathrm{TAG}_{i_{\mathrm{back}}} \times \overline{\mathrm{EM}}_{\mathrm{front}} \tag{3}$$

is generated within 100 ns from the occurrence of an event. A coincidence of a left and right IH hit with a backing tagger hit is required, and not rejected by the forward e^+e^- veto counters. The main trigger

$$\mathcal{MT} = \mathcal{PT}\, OH_L\, OH_R \sum_{i=1}^{32} \mathrm{TAG}_{i_{\mathrm{front}}} \times \overline{\mathrm{inhibit}} \tag{4}$$

requires the coincidence of the pretrigger with a left and right OH hit and a forward tagger hit, not rejected by the computer inhibit signal. A window of 400 ns is available between the $\mathcal{PT}$ and the $\mathcal{MT}$, after which the CAMAC is cleared for the next $\mathcal{PT}$. Typical counting rates are 2 kHz and 30 Hz for the $\mathcal{PT}$ and $\mathcal{MT}$, respectively.

The calibration of the scintillation counters and the CDC and SDC have been the subject of extensive effort [20,29,31]. More recently, a series of modifications implemented in the track fitting algorithms has resulted in significant improvements, mainly in the planar-momentum resolution [32]. It is the tracking that is discussed next.

The CDC consists of four groups of three-wire layers (Fig. 1). The last layer of wires for each group was intended for charge division readout and had not been employed in the past [20]. Instead, hits from the eight remaining CDC layers were used for the reconstruction of the planar momentum p_{xy}, emission angle θ_{sc}, and vertex position (see also Sec. III B). This earlier eight-layer tracking procedure did not incorporate the SDC information either, thus resulting altogether in a less-than-optimal momentum resolution. Since longer effective lengths of reconstructed tracks result in higher-quality fits, however, time-to-digital converter (TDC's) from the last layer of wires of the fourth group have been implemented for the first time in the present analysis. Furthermore, the SDC data have also been used for the first time, a combination which yields an overall improvement in the planar momentum resolution estimated to be $\sigma_{p_{xy}}/p_{xy} = 0.0892 p_{xy} + 0.0057$, compared with $\sigma_{p_{xy}}/p_{xy} = 0.1150 p_{xy} + 0.0078$ from the eight-layer CDC analysis [32]. For a particle of $p_{xy} = 300$ MeV/c, this amounts to a 40% improvement in the planar momentum resolution. The corresponding improvement in the vertex position is reflected in Fig. 2, and has allowed for more stringent tests in the selection of two-track events which originate from the target area. A minor improvement has also been noted in the emission angle resolution, which stays relatively constant at $\sigma_\varphi \sim 0.3°$ throughout the range of typical planar momenta 100 MeV/$c \leqslant p_{xy} \leqslant 500$ MeV/c [32].

The steps involved in the tracking of trajectories through the SDC and CDC may be summarized in the following: The CDC TDC's operate in ''common-stop'' mode, with the start determined from each CDC sense wire and the stop from the

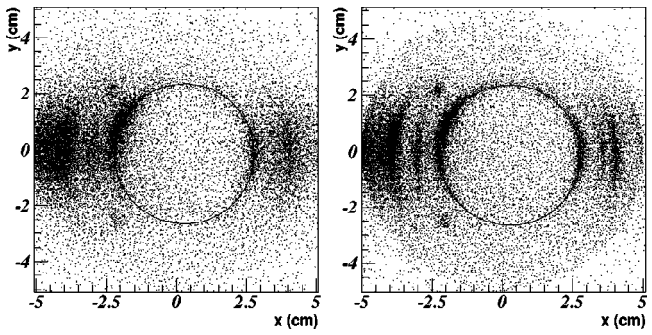

FIG. 2. The vertex position is plotted, reconstructed from the eight-layer CDC data only (left panel), and from the nine-layer CDC and SDC data (right panel), for a set of empty-target runs [32]. The evident improvement in the resolution is discussed in the text. The components of the target vessel, visible in the figure, have been discussed elsewhere [29,30]. The inner ring corresponds to the Mylar wall containing the liquid ^{3}He target, a cylinder 50 mm in diameter. A circle indicating the position of the target container has been drawn, centered at $(x,y)=(2.8\ \text{mm}, -1.5\ \text{mm})$ in the TAGX coordinate frame.

IH [20]. The CDC drift times are first corrected by the corresponding TDC timing offsets. The drift-length to drift-time relation is determined next, per layer of CDC wires, as a fifth-order polynomial. This is an iterative process, where an initial set of parameters is used to reconstruct a sample of well-defined high-momentum tracks. The reconstructed trajectories yield a new set of parameters, and the procedure is repeated until the convergence condition is reached, namely, that the residual root mean square (RRMS) improvement over the final two cycles is no better than 0.5%.

Once a CDC track has been reconstructed, a similar procedure is followed for the SDC, where first the TDC timing offset is determined, and subsequently a SDC length-to-time relationship is extracted. This accomplished, ''best'' SDC tracks are identified, which qualify as candidate extensions of a selected CDC track. Typically, two to four SDC tracks are selected as possible extensions of a reconstructed CDC track when all four SDC layers have registered a hit, to a maximum of eight candidate tracks if one SDC layer is missed. The SDC tracks are approximated by straight-line segments, since the error in the position of even the slowest particles which may be expected to result in valid two-track events is within the 150 μm tolerance of the SDC. Finally, the SDC candidates are matched with the CDC reconstructed track, by requiring the minimal CDC + SDC RRMS of the combined track.

The obtained TOF resolution σ_t is better than 380 ps [20]. The TOF is used for particle identification, as well as for the determination of the particles' OH position (along the $\hat{z}$ axis in the TAGX frame as shown in Fig. 1).

III. DATA ANALYSIS

The data presented in this report were collected in two periods, with ^{3}He- and empty-target measurements in each. The superior quality of the photon beam, and a longer running period, resulted in better statistics and a higher ratio of $\pi^+\pi^-$ to accidental triggers for the second phase. This is reflected in the tagger efficiencies and radiator out/in ratios, defined in Eq. (2), which during the later part of the experiment were generally improved. A total of 16,366 $\pi^+\pi^-$ events have been identified from the analysis of two-track events, comprising 73% of the total number of reconstructed events, the remaining being of three (23%) or more tracks ($<4\%$). With the extraction of the $\pi^+\pi^-$ yield Y, the total cross section σ_T is determined from the relation

$$\sigma_T=\frac{Y}{N_T N_\gamma \eta_{\pi^+\pi^-}\eta_{\text{daq}}}, \tag{5}$$

where N_T (nuclei/cm^2) is the ^{3}He target density seen by the photon beam, and N_γ is the incident photon flux. The efficiencies η_{daq} and $\eta_{\pi^+\pi^-}$ account for the data-acquisition live time and $\pi^+\pi^-$ detection efficiencies. The latter, which is in the range of 2.7–6.8 % for the ρ^0 channels, is determined by dedicated MC routines and is reaction-channel specific (see Ref. [20]).

A. Empty target background

In Sec. II A, the extraction of the tagger efficiencies and the normalization of the tagger scalers to reflect the number of photons incident on the target were discussed. These are utilized in determining the appropriate factor by which empty-target spectra are scaled prior to their subtraction from the corresponding ^{3}He-target spectra, for the removal of target background counts. The procedure is briefly summarized in the following steps.

At regular intervals throughout each of the ^{3}He-target and empty-target running periods, the lead-glass Cerenkov counter is employed in dedicated reference runs to determine the quantities η_l and $\mathcal{R}_l$, as described in Sec. II A. The total number of photons incident on the target per experiment is extracted as the sum of the raw scaler counts T_l, recorded for each run, corrected by the efficiency and out/in ratios for that run, according to Eq. (2), and weighted by the normalized energy distribution of the scattered electrons. In particular, η_l and $\mathcal{R}_l$ for each run are calculated from the corresponding quantities of the reference runs, on the assumption that they vary linearly with the raw scaler counts accumulated between runs. The ratios of photon fluxes between each ^{3}He-target and its corresponding empty-target experiment yield the scaling factors by which the latter are normalized prior to subtraction from the former. The x-coordinate spectrum of the two-pion crossing vertex after background subtraction, indicative of the accuracy of this procedure, is shown in Fig. 3.

B. Experimental observables

The calibration procedure, discussed in Sec. II C, allows the extraction of the planar momentum p_{xy}, the polar emission angle in the median plane φ, the planar trajectory length l_{xy} from the SDC+CDC particle tracking, and the time of flight and z coordinate (OH position) from the IH and OH scintillators:

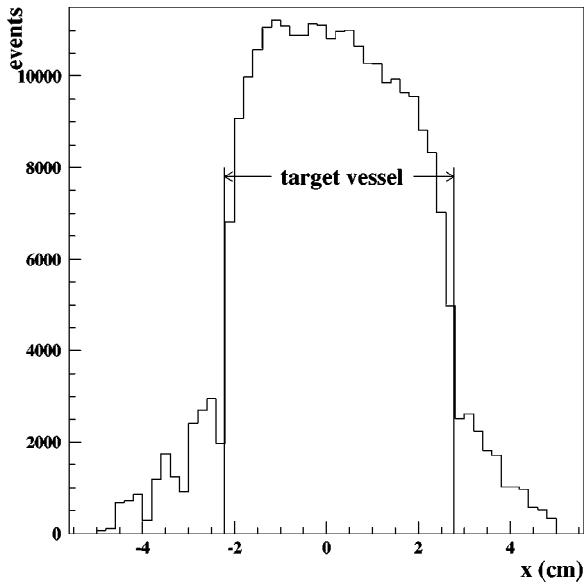

FIG. 3. The x coordinate of the vertex position after background subtraction is shown, along with the target-vessel walls indicated as lines. Only $\pi^+\pi^-$ events from this target region are considered in the analysis.

$$t=\frac{1}{2}(t_{\mathrm{OH}}^{\mathrm{up}}+t_{\mathrm{OH}}^{\mathrm{down}})-t_{\mathrm{IH}},$$

$$z=\frac{1}{2}(t_{\mathrm{OH}}^{\mathrm{down}}-t_{\mathrm{OH}}^{\mathrm{up}})v_{\mathrm{eff}}. \tag{6}$$

The up-down indices correspond to the timing measurements at the two ends of the OH, and v_{eff} is the effective light transmission velocity in the scintillator material. These yield the primary observables (Figs. 4 and 5)

$$\theta_{\mathrm{dip}}=\tan^{-1}\left(\frac{z}{l_{xy}}\right),$$

$$p=p_{xy}/\cos\theta_{\mathrm{dip}},$$

$$l=l_{xy}/\cos\theta_{\mathrm{dip}},$$

$$\beta=l/ct,$$

$$m=p/\beta\gamma c,$$

$$\theta_{\mathrm{sc}}=\cos^{-1}\left(\cos\varphi\frac{p_{xy}}{p}\right), \tag{7}$$

where θ_{dip} is the out-of-plane dip angle, p and l the total momentum amplitude and three-dimensional trajectory length, and θ_{sc} the scattering angle with respect to the incident beam (Fig. 5). A left-right asymmetry noted in the scattering angle θ_{sc} spectrum [Fig. 5(d)] has been reproduced in the MC simulations.

A coincidence of two charged particles, one on either side of the photon beam, signifies the occurrence of an event (Sec. II C). A series of tests and cuts in the data set subsequently eliminates all but the $\pi^+\pi^-$ pairs. In particular, first

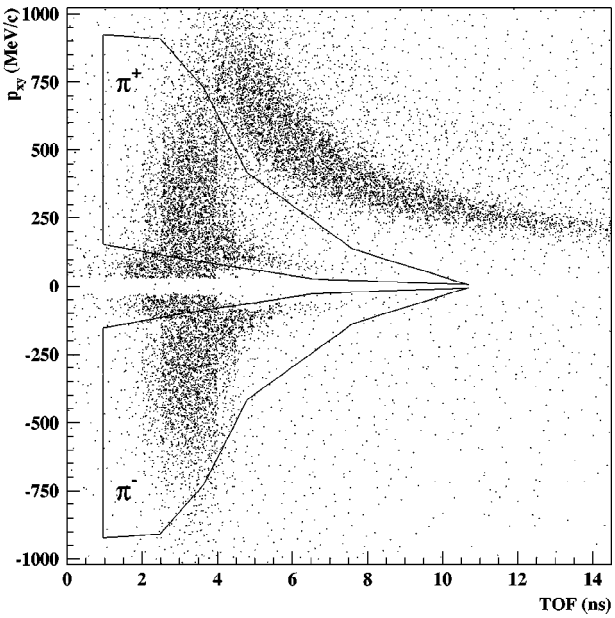

FIG. 4. The TOF-vs-planar momentum spectra, displaying proton (upper-most), $\pi^{\pm}$ (in the box cuts), and $e^{\pm}$ (adjacent to the $p_{xy}=0$ axis) bands, are used for particle identification. The sign of the momentum corresponds to the charge of the particles.

the time-of-flight versus planar momentum spectra are used for particle identification [(PID), Fig. 4]. The great majority of events including a proton or $e^{\pm}$ are thus discarded. Cuts on the tagger TDC spectra reject events induced by spurious photons, not corresponding in timing with the beam pulse. Last, pairs with low-confidence tracks (large RRMS) or whose vertex falls outside the target area (Fig. 2) are elimi-

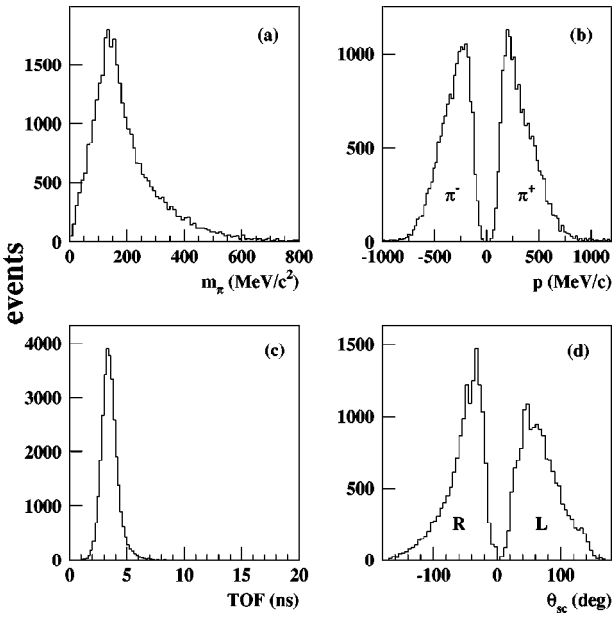

FIG. 5. Some of the kinematical observables for $\pi^+\pi^-$ events, described in the text, are shown. The sign of the momentum corresponds to the pionic charge. The sign of the scattering angle θ_{sc} depends on whether the track registered to the left (>0) or right (<0) of the beam (see Fig. 1).

nated, thus completing a first-level selection based on directly measured observables.

For the two-track events that have cleared the tests above, and have been identified as $\pi^+\pi^-$, additional kinematical observables are calculated. At this stage, the few surviving two-track events involving a proton or $e^{\pm}$ that had been previously misidentified as $\pi^+\pi^-$ by the PID cuts are eliminated as well. The calculated observables include the dipion invariant mass $m_{\pi^+\pi^-}$, the laboratory production angle of the dipion system $\Theta_{\rm IM}$, the missing mass $m_{\rm miss}$ and momentum $p_{\rm miss}$, the π^+-π^- laboratory opening angle $\vartheta_{\pi^+\pi^-}$, and the π^+ production angle in the dipion center of mass $\theta^*_{\pi^+}$, employed as variables in the MC fitting procedure (Sec. IV).

Among these observables, the production angle for either one of the two pions in the dipion center-of-mass frame, for example, $\theta^*_{\pi^+}$, is a unique experimental observable which points to the presence of the ρ^0 production channel well below the nominal threshold energy. This is accomplished without the aid of simulations or assumptions, and is discussed in the next section.

C. $J=1$ signature of the ρ^0

Among the dominant production channels participating in $\pi^+\pi^-$ photoproduction in the $E_\gamma \sim 1$ GeV region (Sec. IV A), only the $\rho^0 \to \pi^+\pi^-$ channel results in two pions being produced at a single reaction vertex with the characteristic $J=1$ angular correlation from the decay of the ρ^0. In the dipion center-of-mass (c.m.) frame, this translates into a $\cos^2\theta^*_{\pi^+}$ distribution, where $\theta^*_{\pi^+}$ is the π^+ production angle with respect to the dipion momentum, the direction defined by the latter in the laboratory frame. This technique, of ρ^0 identification via the study of $\theta^*_{\pi^+}$, has been extensively used in many previous analyses (e.g., Refs. [34,35]), and the $\theta^*_{\pi^+}$ spectrum is expected to be well described as $A + B\cos^2\theta^*_{\pi^+}$ in the vicinity of the dipion invariant mass corresponding to the ρ^0 meson mass, where the $\rho^0 \to \pi^+\pi^-$ amplitude peaks. In other words, this angular distribution is expected to be symmetric around $\cos^2\theta^*_{\pi^+}=0$, on the assumption of a slowly varying $\pi^+\pi^-$ background interfering with the ρ^0 amplitude. Away from the ρ^0 mass, the resonant amplitude vanishes and the background processes dictate the shape of the spectra [33]. This implies that, above and below the ρ^0-meson mass, the angular distribution is expected to follow a quasi-isotropic shape due either to the uncorrelated pions produced at two or more reaction vertices, this being the case for the majority of the participating background processes, or from *s*-wave correlated pions, possibly resulting from the decay of the σ meson (Sec. IV A).

Furthermore, the $\rho^0 \to \pi^+\pi^-$ channel is the only one which results in back-to-back emission of two pions in the dipion c.m. frame. The low Lorentz boost of the dipion c.m. frame, in turn, preserves this large opening angle, between the π^+ and the π^-, in the laboratory frame of reference. Thus, in the examination of $\theta^*_{\pi^+}$ only a single cut was applied to the data, as determined from the MC simulations, which eliminated those $\pi^+\pi^-$ events with too small a laboratory opening angle to have been the outcome of back-to-back emission in the dipion c.m. frame (see Sec. IV B). This cut affects only events from background processes, thereby boosting the $\rho^0 \to \pi^+\pi^-$ amplitude relative to the background (Fig. 6). As such, $\theta^*_{\pi^+}$ is a model-independent observable, free of any assumptions about the process behind each event.

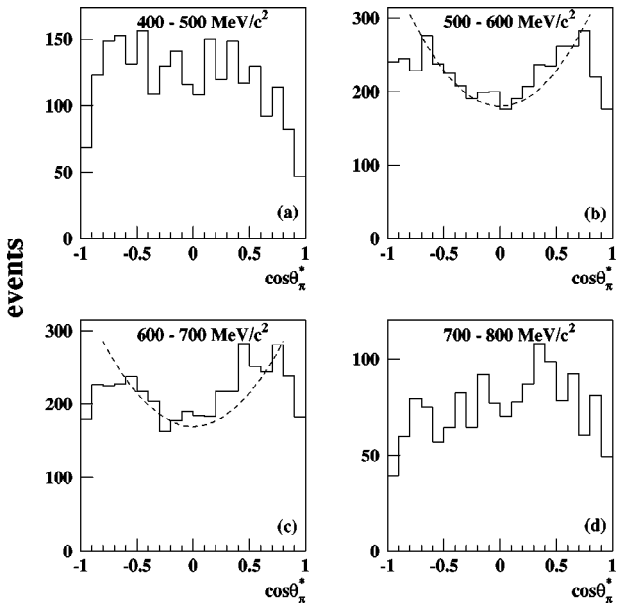

FIG. 6. The $\cos\theta^*_{\pi^+}$ distribution captures the $J=1$ signature of the $\rho^0 \to \pi^+\pi^-$ decay. Panels (b) and (c) display the $A + B\cos^2\theta^*_{\pi^+}$ dependence (dashed curve), expected on the basis of the $J=1$ angular momentum, and the deviation towards ± 1 is due to the spectrometer acceptance.

The $\pi^+\pi^-$ events in the range of 400–800 MeV/c^2 in dipion invariant mass have been divided into four 100 MeV/c^2 bins, which is the finest binning allowed by the data statistics. The 500–600 and 600–700 MeV/c^2 regions [Figs. 6(b) and 6(c)] clearly demonstrate the $J=1$ fingerprint of large opening angle pion pairs resulting from the ρ^0-meson decay. The deviation from $\cos^2\theta^*_{\pi^+}$ toward ± 1 is reproduced in MC simulations of the $\rho^0 \to \pi^+\pi^-$ process, and it is shown to be the effect of the TAGX detection efficiency, stemming from the two-track detection requirement and acceptance restrictions in the forward and backward directions where the photon beam precludes CDC and SDC coverage (see Sec. IV B and Fig. 7). The $\rho^0 \to \pi^+\pi^-$ amplitude, over the 500–700 MeV/c^2 range, points to a substantially reduced ρ^0 mass *beyond* the trivial apparent lowering, which is the artifact of probing the lower tail of the ρ^0 mass distribution with low-energy photons (Sec. V B).

IV. SIMULATIONS

The MC simulations constitute an integral part of the data analysis by determining the process-dependent detection efficiencies of the spectrometer, guiding the assignment of the weight to each of the contributing production mechanisms, and, ultimately, leading to the extraction of the medium-modified ρ^0 mass. The steps involved in the simulations and fitting algorithm can be outlined as follows.

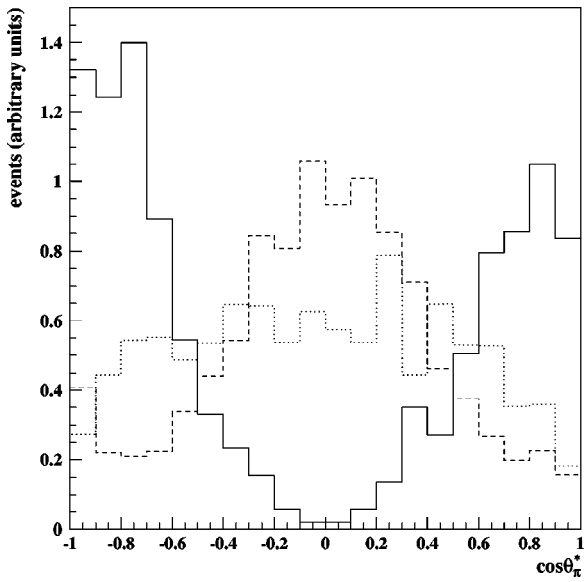

FIG. 7. Simulated events from different processes, taking into account the spectrometer acceptance, have one of three characteristic cos $\theta^*_{\pi^+}$ profiles. The simulations shown are differential cross sections normalized to unity at $E_\gamma = 920$ MeV, and they display the cos $\theta^*_{\pi^+}$ dependence for three representative reactions: (a) $\gamma + {}^3\mathrm{He} \rightarrow \rho^0 ppn \rightarrow \pi^+\pi^- ppn$ with the nominal m_{ρ^0} (solid curve), (b) $\gamma + {}^3\mathrm{He} \rightarrow \pi^- \Delta^{++} pn \rightarrow \pi^+\pi^- ppn$ (dashed curve), and (c) $\gamma + {}^3\mathrm{He} \rightarrow \sigma ppn \rightarrow \pi^+\pi^- ppn$ (dotted curve).

(a) Eleven individual $\pi^+\pi^-$ production channels are coded into MC generators (Sec. IV A). These 11 processes are considered to account for the full $\pi^+\pi^-$ photoproduction yield in the $\gamma + {}^3$He reaction. Twelve distributions of six kinematical observables, with cuts aiming to separate the bound ^{3}He from the dissociated ppn final state, are simulated for each production channel and each of four ΔE_γ energy bins (Sec. IV B). The analysis of the MC events is identical to that of the experimental data, and yields the process-dependent spectrometer acceptance (Sec. IV B).

(b) The simulated spectra for nine of the above elementary processes (Sec. IV A), including background and ρ^0 production channels with the nominal $m_{\rho^0} = 770$ MeV/c^2 mass, are combined. The 12 spectra of each process are adjusted with a common strength parameter within each of the four ΔE_γ bins before being added together. Subsequently, all 12 simulated spectra are fitted simultaneously to the corresponding experimental ones, yielding the nine strength parameters independently for each ΔE_γ bin. From the latter and the spectrometer acceptances, total cross sections are extracted for each of the nine production processes, and compared with independently established ones. Adjustments to the starting values and fitting constraints are made in iterative steps until satisfactory agreement is reached.

(c) The procedure is repeated for these nine production channels, including the addition of two more processes (Sec. IV A) with a modified ρ^0 mass $m^*_{\rho^0}$ in the range 500–725 MeV/c^2, but common for both the ^{3}He and breakup ppn final states. The ρ^0 mass corresponding to the best fit for each ΔE_γ bin is quoted in this report as the medium-modified $m^*_{\rho^0}$ mass (Sec. V A).

(d) Exploratory fits are attempted, decoupling the ^{3}He and breakup ppn final states with respect to $m^*_{\rho^0}$, as well as modifying the width $\Gamma^*_{\rho^0}$ (Sec. V B).

The principal aspects of this algorithm are elaborated below.

A. Production channels

Several mechanisms are known to contribute to $\pi^+\pi^-$ photoproduction. Recent experiments for photon energies between 450 and 800 MeV at MAMI, using the large-acceptance spectrometer DAPHNE and high-intensity tagged photon beams, and in the range 1–2.03 GeV with the SAPHIR detector at ELSA [36], have provided accurate measurements of the reaction $\gamma p \rightarrow \pi^+\pi^- p$ [37–39]. These have motivated several theoretical models, which concur in their interpretation of the data as $\pi^+\pi^-$ photoproduction predominantly through the $\pi\Delta(1232) \rightarrow \pi^+\pi^- N$, and the $N^*(1520) \rightarrow \pi\Delta \rightarrow \pi^+\pi^- N$ channels [40–42]. In the nuclear medium, the propagators of baryonic resonances require renormalization, and, in addition, many-body effects caused by pion rescattering (FSI's) are known to interfere with the lowest-order reaction mechanism of two-pion photoproduction on the nucleon [43]. These medium modifications affect both the strength and the peak position of the cross-section spectra for the various interfering channels, relative to the corresponding processes on a free nucleon. Nonetheless, the $\Delta(1232)$ and N*(1520) resonances remain the leading channels in photon-induced reactions in the nuclear medium, as has recently been verified by total photoabsorption cross-section measurements on nuclei [44]. In the latter, substantial contributions were also attributed to the nucleonic excitations $P_{11}(1440)$ and $S_{11}(1535)$, primarily, which largely overlap with the $D_{13}(1520)$ resonance in medium-modified mass and width.

The double-Δ is another channel that has been verified in photoabsorption measurements on the deuteron [45,46], a process that has also been modeled theoretically [47]. The photon is absorbed on two nuclei, exciting $\Delta(1232)$ resonances in the reaction $\gamma NN \rightarrow \Delta\Delta$, which subsequently decay to produce $\pi^+\pi^-$ pairs.

In addition, three-pion $\pi^+\pi^-\pi^0$ production, associated with ^{3}He disintegration, is kinematically feasible in the energy range probed by the present experiment. However, the limited out-of-plane detector acceptance coupled with appropriate missing-mass cuts minimize the contributions of this mechanism. The experimental measurements available are sparse for this process in the energy regime of interest [37,48,49].

Other possible contributions to the background $\pi^+\pi^-$ yield, which, however, were not found to improve the quality of the fit and are presently not included in the simulations, may come from nonresonant three-, four-, and five-body phase space, corresponding to the ^{3}He remaining intact, or breaking up into dp and ppn, respectively. These multibody phase-space processes are governed solely by energy and momentum conservation, each with a constant transition matrix element [50]. They are, most likely, a superposition of

all the other remaining possible production channels, which are too weak and too broad to be individually identified.

The contributions of the mechanisms discussed so far have been previously considered in MC simulations, in connection with TAGX $\pi^+\pi^-$ photoproduction data [6,21,25]. In Ref. [6] in particular, where $\pi^+\pi^-$ photoproduction via the ρ^0 channel was first considered, the background processes

$$\gamma + {}^3\mathrm{He} \rightarrow \left\{ \begin{array}{ll} \text{(i)} & \Delta\pi(NN)_{\mathrm{sp}} \\ \text{(ii)} & N^*(1520)(NN)_{\mathrm{sp}} \rightarrow \Delta(1232)\pi(NN)_{\mathrm{sp}} \\ \text{(iii)} & N^*(1520)\pi(NN)_{\mathrm{sp}} \\ \text{(iv)} & \Delta\Delta N_{\mathrm{sp}} \\ \text{(v)} & ppn\pi^+\pi^-\pi^0 \end{array} \right\} \rightarrow ppn\pi^+\pi^-$$

were included in simulations of non-ρ^0 $\pi^+\pi^-$ contributions, as well as final state interactions following the ρ^0 decay [see process (ix) below]. The index ''sp'' signifies spectator nucleons. The empirical values from Ref. [44] were used for the $\Delta(1232)$ mass and width and for the $N^*(1520)$ mass, but the fit improved with the $N^*(1520)$ width doubled relative to Ref. [44]. This *ad hoc* increase effectively incorporates the nearby resonances $P_{11}(1440)$ and $S_{11}(1535)$, which largely overlap with the $D_{13}(1520)$, but cannot be resolved within the sensitivity of the data. Alternate fits were performed with the $N^*(1520)$ replaced by the Roper $N^*(1440)$ and including five-body phase space. The two methods yield comparable masses for the ρ^0, but the former is preferred as it results in a better fit.

Additional improvements in the fitting procedure, relative to the analyses of Refs. [6,21,25], include the modification of the MC generators to account for the angular momentum of all $\rho^0 \rightarrow \pi^+\pi^-$ and intermediate-Δ-resonance channels. Furthermore, motivated by recent $\pi\pi$ phase-shift analyses, which increasingly show evidence of *s*-wave contributions from the σ meson, the quasifree σ-decay channel

$$\text{(vi)} \qquad \gamma + {}^3\mathrm{He} \rightarrow \sigma ppn \rightarrow \pi^+\pi^- ppn$$

has been added, with the σ mass and width parameters from Ref. [51].

Last, $\rho^0 \rightarrow \pi^+\pi^-$ photoproduction has been simulated by means of five distinct generators, namely,

$$\gamma + {}^3\mathrm{He} \rightarrow \left\{ \begin{array}{lll} \text{(vii)} & \rho^0 + {}^3\mathrm{He} \rightarrow \pi^+\pi^- {}^3\mathrm{He} & \left. \begin{array}{l} \\ \\ \\ \end{array} \right\} m_{\rho^0} = 770 \ \mathrm{MeV}/c^2, \\ \text{(viii)} & \rho^0 ppn \rightarrow \pi^+\pi^- ppn & \\ \text{(ix)} & \rho^0 ppn \rightarrow \pi^+\pi^- ppn + (\mathrm{FSI}) & \\ \text{(x)} & \rho^0 + {}^3\mathrm{He} \rightarrow \pi^+\pi^- {}^3\mathrm{He} & \left. \begin{array}{l} \\ \\ \end{array} \right\} 500 \ \mathrm{MeV}/c^2 \leqslant m^*_{\rho^0} \leqslant 725 \ \mathrm{MeV}/c^2, \\ \text{(xi)} & \rho^0 ppn \rightarrow \pi^+\pi^- ppn & \end{array} \right.$$

where to channels (vii)–(ix) and (x),(xi) are ascribed ρ^0 decay outside and inside the nuclear medium, respectively, the latter probing the medium effect on the ρ^0 mass. The breakup channels have the reaction taking place on a single nucleon, subject to its Fermi motion, with the remaining two nucleons as spectators. Final state πN interaction with one of the two spectator nucleons is included in channel (ix). Simulations of FSI's in the background (non-ρ^0) processes were not performed, as they bear no qualitative effect on these processes other than to dilute the features of their distributions, and, in any event, are not necessary for an estimate of the background. A lengthier discussion of FSI effects is presented in Sec. V A.

B. Fitting procedure

In modeling $\pi^+\pi^-$ photoproduction on nuclei, the distributions of five kinematical observables (Sec. III B) were simultaneously fitted to the data in Refs. [6,21,25]. These are (1) the dipion invariant mass $m_{\pi^+\pi^-}$, (2) the laboratory production angle of the dipion system Θ_{IM}, (3) the missing

mass m_{miss}, (4) the missing momentum p_{miss}, and (5) the $\pi^+-\pi^-$ laboratory opening angle $\vartheta_{\pi^+\pi^-}$, to which one additional kinematical observable has presently been added (Sec. III C), namely, (6) the π^+ production angle in the dipion rest frame $\cos\theta^*_{\pi^+}$.

Moreover, in Ref. [21] it was determined that dividing the data sample in $\Delta E_\gamma = 80$ MeV bins provided the optimal compromise between the presumed constancy of the reaction matrix elements, implicit in the MC simulations which only depend on the kinematics, and the requirement of sufficient statistics. The ΔE_γ partitioning of the data is necessary in order to account for the varying energy dependence of the $\pi^+\pi^-$ cross sections from each of the individual production mechanisms. The 80 MeV binning in E_γ has been retained, resulting in four sectors of the data sample from 800 to 1120 MeV, to be referred by their respective central E_γ values (840, 920, 1000, and 1080 ± 40 MeV).

The addition of the $\cos\theta^*_{\pi^+}$ distribution, though not noticeably affecting the overall quality of the fit, nonetheless provides an additional physical constraint which aids the MC fitting algorithm to converge to a more realistic solution. In particular, this kinematical observable uniquely captures a characteristic feature of the contributing mechanisms, which may be classified into three types according to their respective dependence on $\cos\theta^*_{\pi^+}$ (Fig. 7):

(a) The channel of interest, diffractive $\rho^0\to\pi^+\pi^-$, is unique in producing two p-wave correlated pions. The spectrometer response to this mechanism is consistent with the $J=1$ dependence, and the deviation from the anticipated $\cos^2\theta^*_{\pi^+}$ distribution towards $\sim\pm 1$ reflects the acceptance cut, stemming from the kinematical conditions, setup geometry, and the two-pion detection requirement [compare the solid curve of Fig. 7 with Figs. 6(b) and 6(c)].

(b) The background hadronic channels (i)–(iv) of Sec. IV A produce two uncorrelated pions at two or more reaction vertices. The angular correlations of these pions are averaged out over 4π sr in simulations, resulting in featureless $\cos\theta^*_{\pi^+}$ spectra. The spectrometer geometry, however, suppresses the pion acceptance away from $\cos\theta^*_{\pi^+}=0$ (see, e.g., the dashed curve of Fig. 7 for the single-Δ production channel). This is a consequence of the fact that channels (i)–(iv) involve the decay of intermediate baryonic resonances, accompanied by energetic nucleons, which are rejected in the analysis.

(c) Three-pion production and the quasielastic σ process, (v) and (vi) of Sec. IV A, are characterized by featureless $\cos\theta^*_{\pi^+}$ acceptances, as no energetic nucleons are emitted (dotted curve of Fig. 7).

The combination of improvements relative to the analysis of Ref. [6], namely, accounting for the angular momentum in the Δ and ρ^0 channels, and imposing additional physical constraints via the new kinematical observable $\cos\theta^*_{\pi^+}$, resulted in a more accurate treatment of the process-dependent spectrometer acceptances.

The data have been subjected to two additional cuts, one of which enhances the ρ^0 relative to the background channels, and the other facilitates the separation of the bound ^{3}He

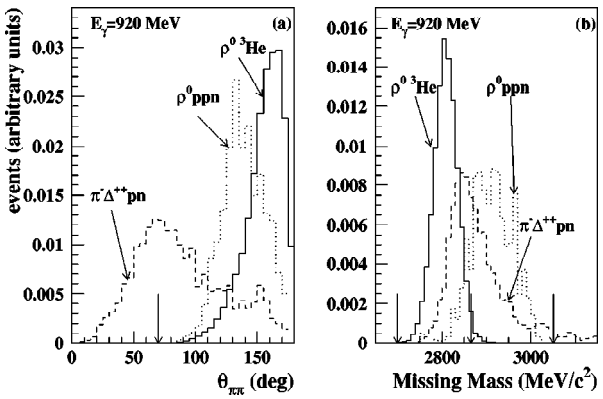

FIG. 8. The effects of the (a) π^+-π^- opening-angle and (b) missing-mass cuts, indicated as arrows in the figure, are shown for the respective simulated spectra of the $\rho^0\,{}^3$He, $\rho^0 ppn$, and $\pi^-\Delta^{++}pn$ channels (solid, dotted, and dashed lines, respectively). The calculations are for $E_\gamma = 920$ MeV and the integral of each distribution is normalized to unity.

from the breakup ppn final states. The former is a $\pi^+\pi^-$ opening-angle cut determined from MC simulations, namely, $70°\leqslant\vartheta_{\pi^+\pi^-}\leqslant 180°$, eliminating two-pion events that could not have been produced back to back from the ρ^0 decay [Fig. 8(a)]. This cut is most effective at the higher end of photon energies covered by the experiment, where the ρ^0 identification becomes difficult by an increasingly deteriorating ρ^0-to-background ratio with increasing E_γ. The latter cut [Fig. 8(b)] separates events with missing mass in the proximity of the target mass $m_{^3\mathrm{He}}\approx 2.8$ GeV/c^2 (i.e., 2700 MeV/$c^2 < m_{\mathrm{miss}} <$ 2865 MeV/c^2), from those associated with the breakup of the target nucleus to ppn in the final state (2865 MeV/$c^2 < m_{\mathrm{miss}} <$ 3050 MeV/c^2). The combination of the two types of cuts is applied to three of the kinematical observables, resulting in six additional spectra, besides the unselected $\pi^+\pi^-$ distributions (1)–(6) enumerated earlier. These are

$$\left.\begin{array}{ll}(7) & m_{\pi^+\pi^-}\\ (8) & p_{\mathrm{miss}}\\ (9) & \cos\theta^*_{\pi^+}\end{array}\right\}\ \rho^0\text{-enhanced low-missing-mass data,}$$

$$\left.\begin{array}{ll}(10) & m_{\pi^+\pi^-}\\ (11) & p_{\mathrm{miss}}\\ (12) & \cos\theta^*_{\pi^+}\end{array}\right\}\ \rho^0\text{-enhanced high-missing-mass data.}$$

While the contributing ρ^0 photoproduction mechanisms may not be experimentally distinguishable (Sec. I), the cuts aim at partitioning the data in biased samples favoring processes which are more prone to probing either the nuclear mean-field effect [i.e., coherent and exclusive quasifree photoproduction via the distributions (7)–(9)] or a possible nucleonic effect [i.e., the breakup quasifree channel via the spectra (10)–(12)]. The three kinematical observables which were subjected to the cuts, namely, the dipion invariant mass, missing momentum, and dipion-c.m. π^+ production angle, were selected empirically from the kinematical ob-

servables (1)–(6) as more sensitive to the ρ^0 mass, and therefore more susceptible to possible medium effects.

With a range of $m^*_{\rho^0}$ values spanning the region 500–725 MeV/c^2, and each value kept common for the unselected, as well as the ^{3}He and ppn selected data, the 12 simulated spectra were fitted simultaneously to the corresponding experimental ones, by minimizing a standard χ^2 function with the strengths of the 11 individual processes (i)–(xi) (Sec. IV A) as the fit parameters. Each of the four $\Delta E_\gamma = 80$ MeV bins was fitted independently from the other three. The optimal $m^*_{\rho^0}$ for each bin is that corresponding to the minimum value of the χ^2 function (Sec. V A).

In summary, the MC fitting procedure satisfies the following requirements.

(a) The $\Delta E_\gamma = 80$ MeV binning restricts the energy dependence of the participating processes to the narrowest bin possible without loss of sufficient statistics.

(b) The six kinematical observables utilized in the fitting are complementary and account for different physical attributes of the data sample. This imposes far more stringent constraints than an analysis based on only the invariant mass distribution, as in the case of the CERES data [7].

(c) The extracted cross sections for the background reactions in Sec. IV A are compared and/or constrained by published or extrapolated cross sections from the literature.

(d) The simultaneous fitting of selected and unselected data aims at isolating a strong signal from data samples most responsive to possible ρ^0 mass modifications, while also incorporating in the fit the bulk of $\pi^+\pi^-$ events produced in processes less sensitive to such effects.

The outcome of this procedure is the medium-modified ρ^0 meson mass.

V. RESULTS

A. Quality of fit and uncertainties

Beyond the statistical and other experimental uncertainties which are folded into the calibration and analysis of the measured $\pi^+\pi^-$ yields, additional sources of uncertainty are generated by the MC simulations and fitting algorithm. (i) The MC event generators depend exclusively on kinematical parameters, assuming a constant production matrix element for each 80 MeV photon energy bin. Thus, other aspects of the interaction are not explicitly included. As an example, the channel $\gamma + {}^3\mathrm{He} \rightarrow (np)_{\mathrm{sp}}\Delta\pi$ is modeled as $\gamma + {}^3\mathrm{He} \rightarrow (np)_{\mathrm{sp}}\Delta^{++}\pi^-$, normalized by an isospin scaling factor to account for the remaining hadronic charge states. This introduces an uncertainty in the amplitude of this process, the type of which is also present in other background hadronic channels. (ii) Independent total cross-section measurements of the constituent reactions, serving to anchor their relative strengths in the full $\pi^+\pi^-$ production process, are sparse (e.g., the quasielastic σ channel). The strength for some of the individual channels was inferred from indirect sources. (iii) Additional quasifree channels and independent measurements to fix their strength are required in order to extract precision cross sections for the background hadronic channels from the data, processes which merit attention on their own behalf. This may become possible following the analysis of three charged-particle events from TAGX experiments, currently in progress.

Despite the caveats above, the medium-modified ρ^0 masses extracted from the MC fitting procedure have remained remarkably stable with respect to variations of the strength parameters of the constituent reactions, within each of the four ΔE_γ bins. This is all the more significant considering that the data are fit simultaneously for 12 spectra of six kinematical observables. In conjunction with the direct $J = 1$ fingerprint discussed earlier, the insensitivity of the fit, within physical constraints, adds confidence to the premise that the medium-modified ρ^0-meson masses extracted from the MC simulations reflect genuine features of the data sample.

One of the concerns voiced over the use of the $\rho^0 \rightarrow \pi^+\pi^-$ channel, instead of the $\rho^0 \rightarrow e^+e^-$ channel to investigate ρ^0 medium modifications, has been the effect of FSI's. Such π-nucleon and π-nucleus interactions can alter the energy and momentum of the detected pion, and may result in a lower invariant mass of the dipion system. Three such π-nucleus interactions are possible for the pion energies in this work: (a) π-N elastic scattering, (b) π-N inelastic scattering, and (c) pion absorption on a pair of nucleons. Pion absorption and charge exchange will simply remove the pion from the final state, thus eliminating the event from the analysis. Since the extraction of the final $m^*_{\rho^0}$ does not depend on the total cross section of the process, pion absorption does not alter the conclusions. Inelastic pion scattering will produce at least another pion and missing mass cuts will eliminate such events from further analysis. The only pion interactions which may manifest themsleves in the final $\pi^+\pi^-$ event samples as FSI's are π-N elastic scattering, as

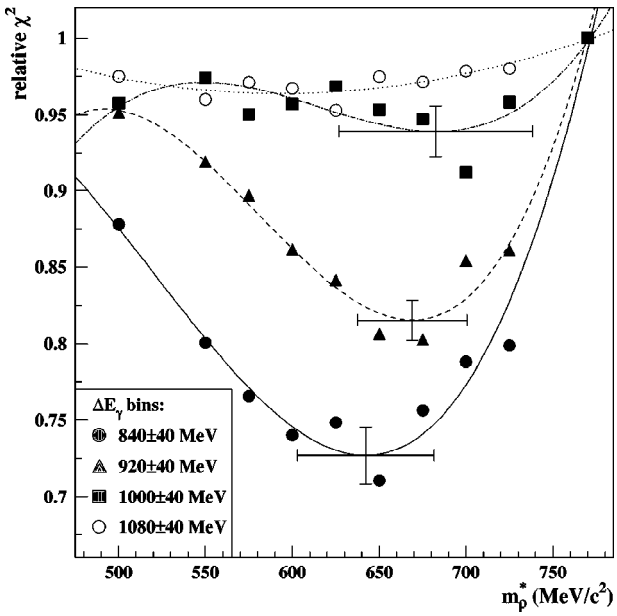

FIG. 9. The dependence of the χ^2 function of the MC fits on the variation of the ρ^0 mass is shown for the four $\Delta E_\gamma = 80$ MeV bins. The MC calculations are indicated as points, and fits to third-order polynomials as curves. The fitting procedure yields the best $m^*_{\rho^0}$ per ΔE_γ bin, and estimates of the respective uncertainties.

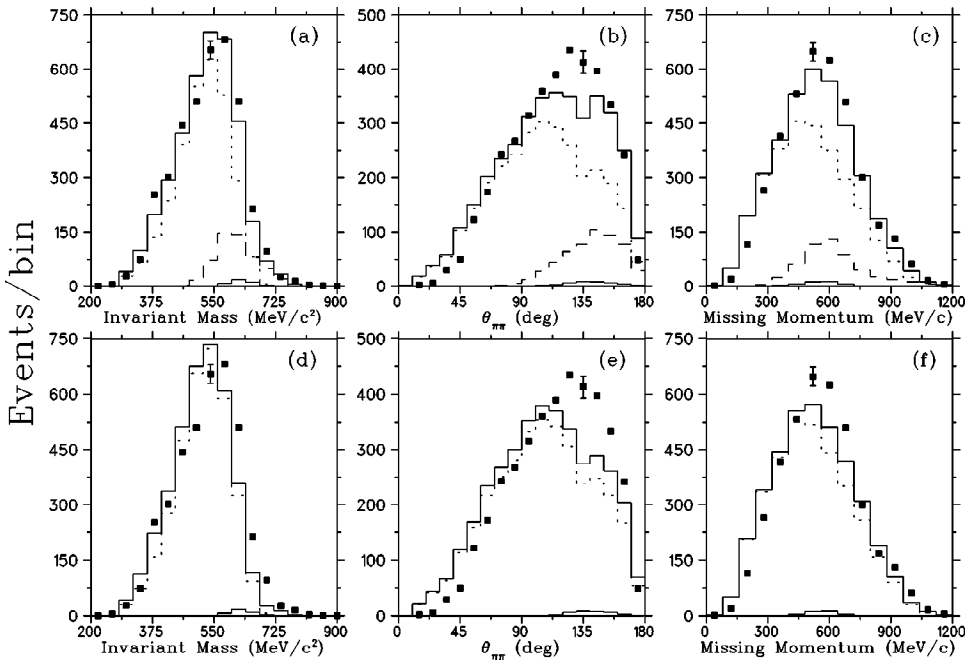

FIG. 10. The dipion invariant-mass [panels (a) and (d)], π^+-π^- laboratory opening-angle [panels (b) and (e)], and missing-momentum [panels (c) and (f)] spectra are shown for the full (unselected) data at $E_\gamma = 840$ MeV. The solid squares are the data, showing only one representative error bar for clarity. The remaining error bars are comparable and have been included in the fitting. The MC fits shown are: full reaction (upper solid lines), non-ρ^0 background processes (dotted lines), ρ^0 contributions with unshifted mass (lower solid lines), and ρ^0 contributions with $m^*_{\rho^0} = 650$ MeV/c^2 (dashed lines). The latter are included only in the calculations represented by the top panels (a), (b), and (c). The improvement from bottom to top reflects the effect of including the ρ^0 medium modifications and is even more pronounced for the ρ^0 selected data set, not shown.

simulated in reaction (ix) of Sec. IV A.

The MC simulation of reaction (ix) includes the kinematics of the produced pion from the ρ^0 decay on a randomly selected nucleon from the Fermi distribution of a single nucleon in ^{3}He. Once all the possible incident and final four momenta are considered, the distributions for the invariant mass, missing momentum, and opening angle for this FSI are quite featureless. Thus, even though FSI's remove events from the regions expected from an unperturbed ρ^0 decay, they do not alter the shape of these distributions. In fact, FSI signatures in the distributions bore many similarities to those of the *s*-wave $\pi\pi$ interaction simulated by reaction (vi) in Sec. IV A, but the MC fitting chose the *s*-wave distribution over that of the FSI's on the basis of better overall χ^2.

Finally, the conclusions from the MC fitting procedure and the minimal effect of FSI's are further emphasized by the $J=1$ signature shown in Fig. 6. Any FSI's which would affect the scattered pion four-momentum enough as to result in a lower $m^*_{\rho^0}$, would also destroy the *p*-wave correlation in the $\cos^2\theta^*_\pi$ distribution, since scattering angle and momentum transfer are uniquely related. The fact that the $J=1$ signature is clearly displayed in the invariant mass region of 500–600 MeV/c^2, after implementation of just the simple opening angle cut, is further proof of information originating from the primary ρ^0 decay, free of FSI contamination.

Following the procedure discussed in Sec. IV, several MC fits have been performed with $m^*_{\rho^0}$ taking on values from a mesh in the range 500–725 MeV/c^2 (Fig. 9). The steepness of the χ^2-vs-$m^*_{\rho^0}$ curve is indicative of the sensitivity of the data sample to ρ^0 mass modifications, within each of the four ΔE_γ bins. Using this as a qualitative criterion, the fittings of the 840 and 920 MeV samples, and to a lesser extent of the 1000 MeV sample, have converged to a ''best'' $m^*_{\rho^0}$, whereas the fit for the 1080 MeV bin is essentially insensitive to variations of $m^*_{\rho^0}$ (Fig. 9).

For each of the 840, 920, and 1000 MeV bins individually, the MC fits (dark circles, triangles, and squares, respectively, in Fig. 9) yield the best $m^*_{\rho^0}$ and an estimate of its uncertainty. This is achieved as follows: (a) The uncertainty σ_{χ^2} is assumed common within each bin. This is justified by the fact that both the data set and the reaction matrix elements used by the MC algorithm are common within each bin. (b) A polynomial expansion of the MC χ^2 about $(m^*_{\rho^0}\text{-}m_0)$, with m_0 in the proximity of the apparent minimum, is assumed to describe well the dependence of the former on the latter. Subsequently a new χ'^2 minimization yields the rank and the coefficients of the polynomial. A third-order polynomial gives the best result for the two lower-energy bins, and it is also assumed to provide the best description of the parent population for the 1000 MeV data sample. This procedure also leads to conservative estimates for σ_{χ^2}, in particular 0.019, 0.013, and 0.017 for the 840, 920, and 1000 MeV bins, respectively. (c) The polynomial coefficients and σ_{χ^2} estimates are used to derive the optimal $m^*_{\rho^0}$ and an estimate of its uncertainty for each bin. These are (i) $m^*_{\rho^0} = 642 \pm 40$ MeV/c^2, 800 MeV$\leq E_\gamma \leq$880 MeV, (ii) $m^*_{\rho^0} = 669 \pm 32$ MeV/c^2, 880 MeV$\leq E_\gamma \leq$960 MeV,

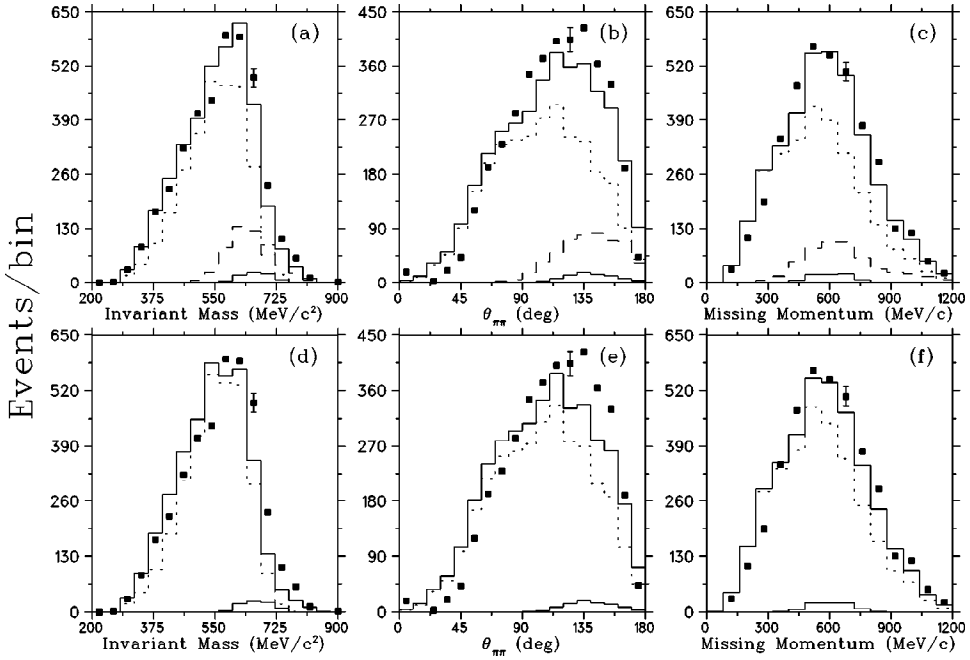

FIG. 11. The data and curves shown are as in Fig. 10, but for the $E_\gamma = 920$ MeV bin, and $m^*_{\rho^0} = 675$ MeV/c^2. It is stressed that the fitting was done independently for each of the four $\Delta E_\gamma = 80$ MeV/c^2 bins, as discussed in the text.

and (iii) $m^*_{\rho^0} = 682 \pm 56$ MeV/c^2, 960 MeV$\leqslant E_\gamma \leqslant$1040 MeV.

The improvement in the medium-modified over the unmodified ρ^0 mass fits is evidenced to varied degrees in all the fitted spectra. The order of the improvement is illustrated for the full (unselected) data in the dipion invariant-mass, π^+-π^- laboratory opening-angle, and missing-momentum distributions for the 840 ± 40 MeV and 920 ± 40 MeV bins, which are most affected by modifications of the ρ^0 mass (Figs. 10 and 11).

The dipion invariant-mass spectra are not the most sensitive to variations of the ρ^0 mass, among the 12 distributions of six kinematical observables that were employed in the fit. This is seen, for example, in comparing the improvement between the unmodified- and modified-mass dipion invariant-mass with the opening-angle and missing-momentum spectra (Figs. 10 and 11), where the latter two observables are seen to display a greater sensitivity. This underlines the advantage of a fitting procedure that utilizes multiple complementary kinematical observables as opposed to only the invariant mass, thus capturing additional attributes of the physical process, and resulting in a more realistic analysis.

B. Discussion

The $J=1$ angular momentum signal, discussed in Sec. III C (Fig 6), as well as the dipion invariant-mass spectrum from the fit [Fig. 10(a)], would appear to indicate medium-modified ρ^0 masses which are actually *lower* than the values quoted earlier [e.g., compare $m^*_{\rho^0} = 642 \pm 40$ MeV/c^2 for the 840 MeV bin with the centroid suggested by the dashed curve of Fig. 10(a)]. This apparent discrepancy is misleading, and has its origin in a trivial effective mass lowering driven by phase space, most pronounced at lower photon energies. This is due to the fact that, at low photon energies, only the lower wing of the ρ^0 mass distribution is kinematically accessible [see Fig. 12(a)]. The shape and the centroid of the mass distribution for the resulting ρ^0 mesons are primarily dictated by the kinematics, and to a lesser extent by the spectrometer acceptance for the particular ρ^0-producing

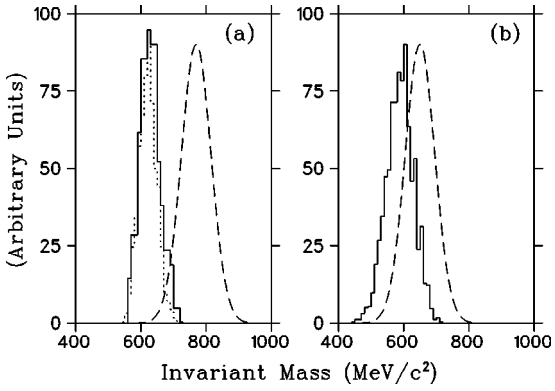

FIG. 12. The trivial ρ^0 mass shift due to kinematic phase-space limitations is illustrated for the quasifree $\gamma + {}^3\mathrm{He} \rightarrow \rho^0 ppn \rightarrow \pi^+\pi^- ppn$ process at $E_\gamma = 840$ MeV, (a) for the nominal and (b) for a lowered ρ^0 mass. The MC generator randomly selects ρ^0 masses from the Gaussian distributions (dashed curves). A Lorentzian ρ^0 mass distribution was also attempted, but was found to yield almost identical results, due to the dominance of kinematic phase-space effects in this subthreshold region. The solid curves are the resulting m_{ρ^0} spectra whose integrals are normalized to unity, after verification that the reaction is kinematically feasible with the selected mass and that the photoproduced pions are accepted by the spectrometer. The dotted curve in panel a) is the result of a simulation of the $N^*(1520) \rightarrow N\rho^0$ decay, at the nominal mass of the ρ^0.

process. This effect is implicit in the MC-generated ρ^0 spectra, and it is by no means sufficient to account for a mass lowering of the order explicitly observed in the experiment. This is manifest, for example, in comparing the lower solid curve of Fig. 10(a) with the $J=1$ fingerprint of the ρ^0 in Fig. 6. The locus of the former curve, consistent with the mass distribution indicated by the histogram of Fig. 12(a) for the nominal ρ^0 mass, is far too high to be compatible with Fig. 6, with a ρ^0 signal peaking in the range of 500–600 MeV/c^2. In contrast, the histogram of Fig. 12(b) for a lowered ρ^0 mass and the dashed curve in Fig. 10(a) are consistent. Furthermore, even the formation of a ''rhosobar'' via the $N^*(1520)N^{-1}$ particle-hole state cannot result in an apparent invariant mass consistent with the data, without modifying the ρ^0 mass. This is also shown in Fig. 12(a), where the invariant-mass distribution of a free ρ^0 (solid line) is indistinguishable from that of a ''rhosobar'' with the vacuum value of 770 MeV/c^2 (dotted line).

Alternate fits were also attempted, to possibly discern additional features from the 840 and 920 MeV bin samples. Decoupling the exclusive ^{3}He from the breakup ppn final states, with respect to $m^*_{\rho^0}$, yielded identical masses for the 920 MeV bin and a somewhat smaller mass for the latter relative to the former channel for the 840 MeV bin. The resulting improvement in the quality of fit, however, is within the uncertainty estimate of σ_{χ^2}.

The effect of a possible width modification in nuclear matter was also investigated. Simulations were performed with $\Gamma^*_{\rho^0}$ fixed to the predicted width at half nuclear density extracted for ^{3}He from Ref. [14], which is 2.3 times as large as the free width Γ_{ρ^0}. These simulations resulted in a sizable improvement in χ^2 with this modified width for any modified ρ^0 mass, compared to the free mass and width case. In all cases, however, the χ^2 is consistently 5–10 % larger with $\Gamma^*_{\rho^0}$ than with the vacuum value of Γ_{ρ^0} for a given m^*_ρ. This consistency indicates that there is no preference in the data for a large width modification for ^{3}He. Equally important, however, is the finding that within the uncertainty in $m^*_{\rho^0}$ generated by such a large $\Gamma^*_{\rho^0}$, the preferred $m^*_{\rho^0}$ is no different than the modified mass obtained when assuming the free width. This means that a χ^2 minimization on the same data set yields effectively the same reduced-mass value, independently of the assumed $\Gamma^*_{\rho^0}$. In summary, these exploratory fits verify the preference for a reduced ρ^0 mass, but are inconclusive, within the sensitivity of the data, as to whether a width modification is supported *in addition*. This conclusion is reinforced further by the $J=1$ signature as a function of the dipion invariant mass (Fig. 6), which points to a well-localized signal, contrary to what one would expect if the width $\Gamma^*_{\rho^0}$ was dramatically increased.

The absence of a conclusive ρ^0 mass-modification dependence from the 1000 and 1080 MeV bins, in contrast to the strong signal from the 840 and 920 MeV bins, is telling as well. Whereas the former are more prone to probing the exclusive channel, and therefore the nuclear mean-field medium effect, the latter are deeper into the subthreshold region, dominated by the breakup channel, and probe distances

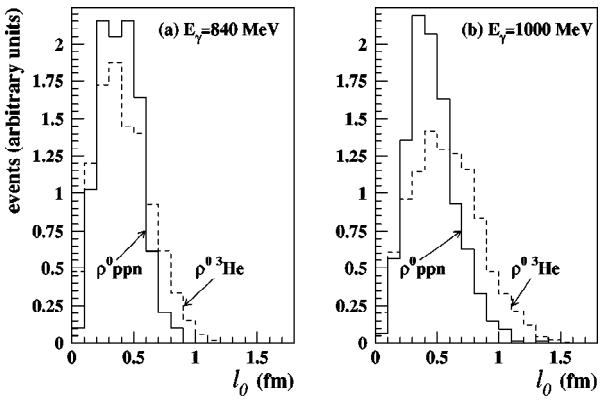

FIG. 13. The mean decay length l_0 distribution, of the $\rho^0 \rightarrow \pi^+\pi^-$ decay, is indicative of the distances probed for vector-meson modifications in this experiment. The l_0 spectra are illustrated for (a) $E_\gamma=840$ MeV and (b) $E_\gamma=1000$ MeV. The histograms are for MC-generated events accepted by the spectrometer in the $\gamma+{}^3\mathrm{He}\rightarrow\rho^0 p(pn)_{\mathrm{sp}}\rightarrow\pi^+\pi^- p(pn)_{\mathrm{sp}}$ (solid curves) and $\gamma+{}^3\mathrm{He}\rightarrow\rho^0\,{}^3\mathrm{He}\rightarrow\pi^+\pi^-\,{}^3\mathrm{He}$ (dashed curves) reactions, with their integrals normalized to unity. The mean decay length is for the former reaction in the rest frame of the participating proton (the two remaining nucleons being spectators), and for the latter in the rest frame of the ^{3}He nucleus.

shorter than the nucleonic radius. One possible exception to this general statement is the effect of a bound ρ^0 decaying within the nucleus, in which the ^{3}He nucleus breaks up into a $\pi^+\pi^- ppn$ final state. To illustrate the range of the ρ^0 processes in different energy regions, we consider the mean decay length l_0 of the ρ^0,

$$l_0=\beta t_0=\frac{p\hbar}{m_{\rho^0}\Gamma_{\rho^0}c},$$

$$\beta=\frac{p}{m_{\rho^0}\gamma c},$$

$$t_0=\gamma\tau_0=\gamma\frac{\hbar}{\Gamma_{\rho^0}}, \tag{8}$$

with the nominal mass m_{ρ^0} and width Γ_{ρ^0} for the ρ^0 meson, in the rest frame of either the interacting nucleon, or the ^{3}He nucleus, for the breakup or bound final states, respectively (Fig. 13).

At low photon energies [e.g., $E_\gamma=840$ MeV, Fig. 13(a)] the ppn channel dominates ρ^0 photoproduction. This is verified by the fact that the low-missing-mass selected data represent less than 10% of the total unselected events, whereas the high-missing-mass selected data contribute the great majority of the ρ^0 events and their corresponding distributions are generally consistent with the full (unselected) data. With the ρ^0 mesons produced on the nucleon, and a mean decay length of under 0.5 fm for a substantial portion of them, there is a large overlap of the volume traversed before their decay and the nucleonic volume. To the extent that the medium modifications of the vector-meson properties depend on the density of the surrounding nuclear matter, it is conceivable that the induced medium effect is dominated by the large densities encountered in the interior of the nucleon. Conversely, it is easy to see why such a dynamical ρ^0-nucleon

geometry will also enhance the probability of the formation of a ''rhosobar,'' which is perhaps an alternate way of expressing the same nucleonic nature of the ρ^0-nucleon interaction at lower photon energies.

At higher photon energies [e.g., $E_\gamma = 1$ GeV, Fig. 13(b)] the mean decay length increases. Whereas nucleonic densities become increasingly inaccessible, a large overlap of the volume traversed by the ρ^0, before its decay, with the ^{3}He nucleus, may still induce a weaker nuclear medium effect. Moreover, the possibility of a medium-induced increase in the width Γ_{ρ^0} is in favor of shorter decay lengths [Eq. (8)], and therefore further increases the likelihood of accessing regions of large densities either in the nucleon or the nuclear core. The present results may therefore be suggestive of a moderate medium effect in the realm of the nuclear mean field at near-threshold photon energies, probing normal nuclear densities, turning to a drastic reduction of the ρ^0 mass in the deep subthreshold region, where the ρ^0 decay may be induced in the proximity of the nucleon. These implications, however, need to be further investigated and verified by higher precision and large solid angle experiments [28], where different signatures of various processes, such as bound states [23], tensor coupling [24], and nucleonic effects [27], may be separated and identified.

VI. CONCLUSIONS

In summary, the kinematics and final state of the $^3\mathrm{He}(\gamma,\pi^+\pi^-)X$ reaction have been studied with the TAGX spectrometer and a tagged photon beam in the subthreshold ρ^0 photoproduction region. The bound ^{3}He and breakup ppn components of the ρ^0 channel have been investigated, aiming at the distinction between a nuclear and a possible nucleonic medium effect on the ρ^0 mass. The ρ^0 channel has been aided by the inherent selectivity of the TAGX spectrometer to $\pi^+\pi^-$ events from the $\rho^0 \rightarrow \pi^+\pi^-$ decay and by the choice of ^{3}He as a target with minimal FSI effects without suppression of the ρ^0 amplitude. In any case, the size of target appears to have little effect in the subthreshold region. The $J=1$ fingerprint of the ρ^0 has been observed in the dipion invariant-mass region 500–700 MeV/c^2, pointing to a substantial reduction beyond a trivial, phase-space-governed, apparent lowering. This has been verified by MC simulations, incorporating the exclusive and breakup ρ^0 channels, the latter both with and without FSI's, as well as background hadronic channels and *s*-wave correlations.

The extracted ρ^0 medium-modified masses, 642 ± 40, 669 ± 32, and 682 ± 56 MeV/c^2 for the 840, 920, and 1000 MeV data bins suggest a strong medium effect in the deep subthreshold region, requiring large densities that are incompatible with a nucleus as light as ^{3}He, but that are more consistent with the probing of the nucleonic volume. It is clear that the observed effect is not a simple kinematic shift nor an unmodified ''rhosobar.'' Whether it is a hadron density effect, an additional element in the ρ^0-nucleon coupling, or a ρ^0 bound state in ^{3}He, the fact remains that a substantial lowering of the ρ^0 mass is required by the experimental results.

The extent of this apparent mass modification, which is independently supported by the assumption-free experimental $J=1$ signature, is substantially beyond typical predictions of most mean-field models. Whereas modest mass modifications that have been put forward by the latter models may arguably be attributed to phenomenological (hadronic) medium effects, which affect the spectral function and ρ^0 width in the nuclear medium but induce minimal modifications to the ρ^0 mass itself (Sec. I), this work points to a different, unexplored as yet, mechanism at play. Though the simulations are inconclusive regarding the size of a possible medium-induced modification of the ρ^0 width, any such modification up to the extreme case of doubling the vacuum width has practically no effect on the preferred ρ^0 masses. The lack of sensitivity of the data to a width modification, in conjunction with the range of the ρ^0 mesons that appears to be compatible with the nucleonic size in the deep subthreshold region, seems to suggest an effect which might be most appropriately formulated in terms of quark degrees of freedom.

In the absence of a well-established theoretical framework, the discussion of a possible nucleonic effect in this work has been kept in the more familiar, though perhaps less accurate, terms of a medium effect where the nucleonic mass distribution takes up the role of the nuclear medium. Clearly, if such an effect is verified, quark degrees of freedom will inevitably provide a more physical description in processes with a range below 0.5 fm. The pattern of decreasing sensitivity with increasing photon energy, with the 1080 MeV bin showing no evidence of a ρ^0 mass-modification signal, hints at a moderate mean-field nuclear effect at near-threshold energies, which could be understood in terms of more conservative, hadronic-phenomenological models.

Further analysis, currently in progress, for photoproduction on both heavier and lighter targets (^{12}C, ^{2}H) and for background contributions (e.g., the $\Delta\pi$ channel) from TAGX experiments, as well as future experiments planned for TJNAF [28], may more accurately isolate the $\rho^0 \rightarrow \pi^+\pi^-$ channel from the background processes, and shed light on the nature of the medium modifications on light vector-meson properties at the interface of hadronic and quark matter. The foremost limitations, which hampered the overall agreement of the fits with the observed distributions in the analysis presented in this paper, are believed to be an inaccurate knowledge of the process-dependent acceptances inherent for the TAGX spectrometer, as well as a coarse tagged energy affecting the assumed constancy of the relevant matrix elements in the simulated reactions. On both counts, future experiments guarantee an improvement.

ACKNOWLEDGMENTS

The authors wish to thank H. Okuno and the staff of INS-ES for their considerable help with the experiment. Furthermore, the authors acknowledge the very insightful discussions with P. Guichon, M. Ericson, A. Thomas, and A. Williams during the Workshop on Hadrons in Dense Matter (Adelaide, 1997), as well as the discussions with N. Isgur at Jefferson Lab. This work has been partially supported by grants from INS-ES, INFN/Lecce, NSERC, and UFF/GWU.

[1] A. Casher, Phys. Lett. **83B**, 395 (1979).
[2] R. Pisarsky, Phys. Lett. B **110B**, 155 (1982).
[3] T. Hatsuda and S. H. Lee, Phys. Rev. C **46**, R34 (1992).
[4] G. E. Brown, Nucl. Phys. **A488**, 689 (1988).
[5] G. E. Brown and C. M. Rho, Phys. Rev. Lett. **66**, 2720 (1991).
[6] G. J. Lolos *et al.*, Phys. Rev. Lett. **80**, 241 (1998).
[7] CERES Collaboration, G. Agakichiev *et al.*, Phys. Rev. Lett. **75**, 1272 (1995); G. Agakichiev *et al.*, Phys. Lett. B (to be published).
[8] HELIOS-3 Collaboration, M. Masera *et al.*, Nucl. Phys. **A590**, 93c (1995); NA50 Collaboration, E. Scomparin *et al.*, *ibid.* **A610**, 331c (1996).
[9] G. Q. Li, C. M. Ko, and G. E. Brown, Phys. Rev. Lett. **75**, 4007 (1995).
[10] W. Cassing, W. Ehehalt, and C. M. Ko, Phys. Lett. B **363**, 35 (1995); C. P. de los Heros, Ph.D. thesis, Weizmann Institute, 1996.
[11] R. Rapp, G. Chanfray, and J. Wambach, Nucl. Phys. **A617**, 472 (1997).
[12] W. Cassing, E. L. Bradkovskaya, R. Rapp, and J. Wambach, Phys. Rev. C **57**, 916 (1998).
[13] B. Friman and H. J. Pirner, Nucl. Phys. **A617**, 496 (1997).
[14] F. Klingl, N. Kaiser, and W. Weise, Nucl. Phys. **A624**, 527 (1997).
[15] NA50 Collaboration, M. Gonin *et al.*, Nucl. Phys. **A610**, 404c (1996).
[16] G. E. Brown, C. B. Dover, P. B. Siegel, and W. Weise, Phys. Rev. Lett. **60**, 2723 (1998), and references therein.
[17] E. J. Stephenson, J. Liu, A. D. Bacher, S. M. Bowyer, S. Chang, C. Olmer, S. P. Wells, S. W. Wissink, and J. Lisantti, Phys. Rev. Lett. **78**, 1636 (1997).
[18] R. Koniuk and N. Isgur, Phys. Rev. D **21**, 1868 (1980).
[19] K. Saito, K. Tsushima, and A. W. Thomas, Phys. Rev. C **56**, 566 (1997).
[20] K. Maruyama *et al.*, Nucl. Instrum. Methods Phys. Res. A **376**, 335 (1996).
[21] D. G. Watts *et al.*, Phys. Rev. C **55**, 1832 (1997).
[22] H. Alvensleben *et al.*, Nucl. Phys. **B18**, 333 (1970).
[23] Z. Papandreou, G. M. Huber, G. J. Lolos, E. J. Brash, and B. K. Jennings, Phys. Rev. C **59**, 1864 (1999).
[24] A. Bhattacharyya, S. K. Ghosh, and S. Raha, nucl-th/9902060.
[25] G. M. Huber, G. J. Lolos, and Z. Papandreou, Phys. Rev. Lett. **80**, 5285 (1998).
[26] G. E. Brown, M. Buballa, and M. Rho, Nucl. Phys. **A609**, 519 (1996).
[27] P. A. M. Guichon and M. Ericson (private communication).
[28] G. J. Lolos *et al.*, ''Medium Modifications of Vector Mesons in the Subthreshold Region,'' JLab Experiment Proposal No. 99-001.
[29] G. Garino *et al.*, Nucl. Instrum. Methods Phys. Res. A **388**, 100 (1997).
[30] M. Harada, S. Kasai, S. Kato, T. Kitami, T. Maki, K. Maruyama, Y. Murata, K. Niki, C. Rangacharyulu, and A. Sasaki, Nucl. Instrum. Methods Phys. Res. A **276**, 451 (1989); S. Kato, T. Kitami, K. Maruyama, Y. Murata, S. Endo, K. Niki, and T. Morita, *ibid.* **290**, 315 (1990); S. Kato, K. Kobayashi, K. Maruyama, H. Okuno, O. Konno, T. Suda, T. Maki, H. Asami, and T. Koizumi, *ibid.* **307**, 213 (1991).
[31] M. Iurescu, M.Sc. thesis, University of Regina, 1997 (unpublished); A. Weinerman, M.Sc. thesis, University of Regina, 1996 (unpublished).
[32] A. Shinozaki, University of Regina TAGX Collaboration Report, 1998 (unpublished).
[33] I. S. Hughes, *Elementary Particles*, 2nd ed. (Cambridge University Press, Cambridge, England, 1985), pp. 201–202.
[34] W. D. Walker, J. Carroll, A. Garfinkel, and B. Y. Oh, Phys. Rev. Lett. **18**, 630 (1967).
[35] M. Arneodo *et al.*, Nucl. Phys. **B429**, 503 (1994).
[36] SAPHIR Collaboration, W. Scwille *et al.*, Nucl. Instrum. Methods Phys. Res. A **344**, 470 (1994).
[37] F. J. Klein, Ph.D. thesis, Bonn IR-96-08, 1996.
[38] A. Braghieri *et al.*, Phys. Lett. B **363**, 46 (1995).
[39] F. Härter, J. Ahrens, R. Beck, B. Krusche, V. Metag, M. Schmitz, H. Ströher, Th. Walcher, and M. Wolf, Phys. Lett. B **401**, 229 (1997).
[40] J. A. Gomez-Tejedor and E. Oset, Nucl. Phys. **A571**, 667 (1994); **A600**, 413 (1997).
[41] L. Y. Murphy and J. M. Laget, Report No. DAPNIA/SPhN 95-42, 1995.
[42] K. Ochi, M. Hirata, and T. Takaki, Phys. Rev. C **56**, 1472 (1997).
[43] S. S. Kamalov and E. Oset, Nucl. Phys. **A625**, 873 (1997).
[44] N. Bianchi *et al.*, Phys. Rev. C **54**, 1688 (1996).
[45] M. Asai *et al.*, Z. Phys. A **344**, 335 (1993).
[46] Y. Wada, for the SAPHIR Collaboration, Particles and Nuclei International Conference, Williamsburg, Virginia, 1996 (unpublished).
[47] J. A. Gomez-Tejedor, E. Oset, and H. Toki, Phys. Lett. B **346**, 240 (1995).
[48] J. Hannappel, Ph.D. thesis, Bonn IR-96-04, 1996.
[49] ABBHHM Collaboration, Phys. Rev. **175**, 1669 (1968).
[50] D. Luke and P. Soding, in *Symposium on Meson-, Photo-, and Electroproduction at Low and Intermediate Energies*, Springer Tracts in Modern Physics Vol. 59, edited by G. Höhler (Springer-Verlag, Berlin, 1971), p. 39.
[51] R. M. Barnett *et al.*, Phys. Rev. D **54**, 1 (1996).